

Comparison of CS, CGM and CS-CGM for Prediction of Pipe's Inner Surface in FGMs

Haolong Chen^{1,2}, Bo Yu¹, Huanlin Zhou^{1*} and Zeng Meng¹

Abstract: The cuckoo search algorithm (CS) is improved by using the conjugate gradient method (CGM), and the CS-CGM is proposed. The unknown inner boundary shapes are generated randomly and evolved by Lévy flights and elimination mechanism in the CS and CS-CGM. The CS, CGM and CS-CGM are examined for the prediction of a pipe's inner surface. The direct problem is two-dimensional transient heat conduction in functionally graded materials (FGMs). Firstly, the radial integration boundary element method (RIBEM) is applied to solve the direct problem. Then the three methods are compared to identify the pipe's inner surface with the information of measured temperatures. Finally, the influences of timepoints, measurement point number and random noise on the inverse results are investigated. It is found that the three algorithms are promising and can be used to identify the pipe's inner surface. The CS-CGM has higher accuracy and faster convergence speed than the CS and CGM. The CS and CS-CGM are insensitive to the initial values. The CGM and CS-CGM are more insensitive to the measurement noises compared with the CS. With the increase of timepoints and measurement points, and with the decrease of measurement noises, the inverse results are more accurate.

Keywords: Inverse geometry problems, transient heat conduction, functionally graded materials, Cuckoo search algorithm, conjugate gradient method.

1 Introduction

In the past several decades, inverse heat conduction problem has been widely applied in the field of science and engineering [Alifanov (1994); Taler and Duda (2006)], such as identification of the boundary conditions [Lee, Lai, Chen et al. (2013); Fu, Chen and Zhang (2012)], thermo-properties [Chen, Chen and Wei (2015)] and geometry of the boundary [Chen, Cao and Wang et al. (2016)] from the knowledge of the temperature measurements taken in the domain or on the surface. The inverse geometry problem (IGP) has broad application in geometry optimization [Naumann, Evans, Walton et al. (2016)], biological lesion detection [Partridge and Wrobel (2007)], radar cross section estimation [Girish and Hema (2016)] and inner surface prediction [Cheng and Chang

¹ School of Civil Engineering, Hefei University of Technology, Hefei, P.R.C.

* Corresponding author: Prof. Huanlin Zhou, zhouhl@hfut.edu.cn.

(2003)]. In the field of engineering, the identification of a pipe's inner-surface shape is of great importance [Fan, Sun and Yang (2007); Mohamed and Marcel (2017)]. Functionally graded materials (FGMs) have attracted many research interests in materials and engineering sciences [Sladek, Sladek and Zhang (2004); Li, Guo, Zhang et al. (2015); Zhang, Yu, Zhang et al. (2015); Wu and Jiang (2015)]. However, the study on the IGP of FGMs is limited in the literature.

Compared with other numerical methods, the boundary element method (BEM) is an effective way to solve the IGP [Li, Wang, Chen et al. (2016)]. The advantage of the BEM to identify boundary shape is that only the boundary is needed to be discretized into elements, which can reduce dimensions and keep accuracy [Sun, Huang, Liu et al. (2004)]. However, the BEM faces a serious challenge when solving non-linear, non-homogeneous and transient problems since there are domain integrals in the resulting integral equations [Abreu, Canelas and Mansur (2013); Tadeu, Prata and Simões (2015); Yu, Zhou, Chen et al. (2015)], thus making the BEM lose its advantage of boundary only discretization. To overcome this shortcoming, the dual reciprocity method (DRM) [Partridge, Brebbia and Wrobel (1992)] and the radial integral method (RIM) [Gao (2002)] have been developed to transform the domain integral into the boundary integral. The RIM can not only transform any complicated domain integrals to the boundary without using the particular solution, but also remove the various singularities appearing in the domain integrals [Gao (2005)]. The method combining RIM with BEM (RIBEM) has been used in non-linear and non-homogeneous elastic problems [Gao, Zhang and Luo (2007)], the heat conduction problems [AL-Jawary and Wrobel (2012)] and thermoelastic problems [Gao, Zheng, Yang et al. (2015)]. Moreover, the boundary particle method [Fu, Chen and Yang (2013)] is suitable to solve the nonhomogeneous problem.

The IGP can be regularized by a series of regularization algorithms, such as the Tikhonov regularization method, the Levenberg-Marquardt method (LMM) and the conjugate gradient method (CGM). Karageorghis et al. (2015) solved the direct and inverse Signorini problems by using the method of fundamental solution. Wang et al. (2015) estimated the geometry boundary for the inner surface in a furnace wall made of FGMs by CGM and finite element method. Kazemzadeh-Parsi and Daneshmand (2013) identified the inner wall of pipeline by using smoothed fixed grid finite elements. Fan et al. (2007) identified a pipeline's irregular inner boundary by the CGM. Hafid et al. (2017) predicted the state of the brick wall of a melting furnace by using the LMM and Broyden method. Different optimization algorithms were also used and compared by Rus et al. (2002). Sun et al. (2016) solved the IGP of a two-dimensional radiative enclosure filling with participating media by the krill herd algorithm.

Generally, many gradient optimization methods have been suggested to solve the IGP, in which LMM and CGM are widely utilized owing to their stable, powerful and efficient characteristics [Huang and Liu (2010)]. However, LMM and CGM are locally convergent and the results are sensitive to the initial values. In practical engineering, it is not convenient to get exact initial values. Especially for complex boundary shape and many observation points, those gradient type algorithms lose efficacy.

In the past several years, evolutionary algorithms have developed quickly and become a

hot topic in structure optimization domain. In 2009, Yang et al. (2009) proposed cuckoo search algorithm (CS). The CS has advantages of good global search capability and few control parameters factors. Yang et al. (2010) applied the CS to solve engineering optimization problems, such as the design of springs and welded beam structures. Up to now, the CS has been widely used in hydrothermal scheduling problems [Nguyen, Vo and Truong (2014)], aerodynamic shape optimizations [Naumann, Evans and Walton (2015)] and reliability optimization problems [Valian, Tavakoli, Mohanna et al. (2013)]. It should be noted that although the CS has good global search ability, its convergence speed is very slow because it does not utilize the gradient information. Thus, it is difficult to apply the CS to complex engineering model due to the unbearable computational cost.

In this paper, the CS is improved by using the CGM, and the CS-CGM is proposed. The CS, CGM and CS-CGM are used and compared to predict a pipe's inner surface in FGMs. A brief outline of the paper is as follows: firstly, the direct problem is solved by RIBEM in Section 2 and the objective function of the inverse problem is proposed in Section 3. The theories of the CS and the CGM are presented and the flowchart of the CS-CGM is shown in Section 4. In addition, numerical examples are presented in Section 5. Finally, some conclusions are drawn in Section 6.

2 Direct problem

2.1 The governing equation

A cross sectional schematic of a pipeline with an irregular inner boundary is displayed in Figure 1. The governing equation for two-dimensional transient heat conduction problems in FGMs is given as follows

$$\frac{\partial}{\partial x_i} \left(\lambda(\mathbf{x}) \frac{\partial T(\mathbf{x}, t)}{\partial x_i} \right) = \rho c \frac{\partial T(\mathbf{x}, t)}{\partial t}, \quad \mathbf{x} \in \Omega, \quad (1)$$

where x_i is the i -th component of the spatial coordinates at point \mathbf{x} . In this paper, $i = 2$. $\lambda(\mathbf{x})$ is the thermal conductivity. $T(\mathbf{x}, t)$ is the temperature at point $\mathbf{x} \in \Omega$ and at time t . ρ and c are the density and the specific heat, respectively.

With the boundary conditions

$$\begin{cases} (T_{in})_{\Gamma_i} = \bar{T}, \\ -\lambda(\mathbf{x}) \left(\frac{\partial T(\mathbf{x}, t)}{\partial \mathbf{n}} \right)_{\Gamma_o} = h(T_{out} - T_\infty), \end{cases} \quad (2)$$

where T_{in} and T_{out} are the temperature on the inner and outer boundary, respectively. T_∞ is the surrounding environment temperature. Γ_i and Γ_o are the inner and outer boundaries. h is the convective heat transfer coefficient.

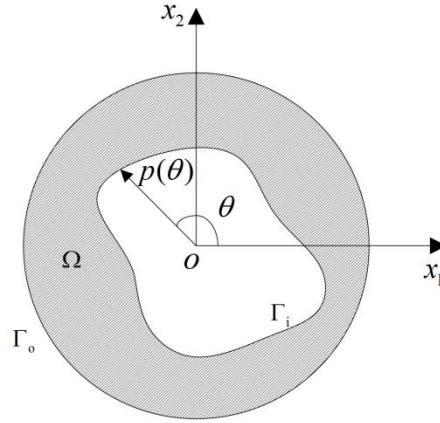


Figure 1: Geometry model

2.2 The direct problem

In order to derive the boundary integral equation, the weight function G is introduced to the Eq. (1). The domain integral equation can be obtained

$$\int_{\Omega} G \frac{\partial}{\partial x_i} \left(\lambda \frac{\partial T}{\partial x_i} \right) d\Omega = \int_{\Omega} G \rho c \frac{\partial T}{\partial t} d\Omega, \tag{3}$$

where $\lambda = \lambda(\mathbf{x})$, $T = T(\mathbf{x}, t)$. Using Gauss's divergence theorem, the left term of Eq. (3) can be manipulated as

$$\begin{aligned} \int_{\Omega} G \frac{\partial}{\partial x_i} \left(\lambda \frac{\partial T}{\partial x_i} \right) d\Omega &= \int_{\Gamma} G \lambda \frac{\partial T}{\partial x_i} n_i d\Gamma - \int_{\Gamma} \lambda T \frac{\partial G}{\partial x_i} n_i d\Gamma \\ &+ \int_{\Omega} T \frac{\partial G}{\partial x_i} \frac{\partial \lambda}{\partial x_i} d\Omega + \int_{\Omega} \lambda T \frac{\partial}{\partial x_i} \left(\frac{\partial G}{\partial x_i} \right) d\Omega, \end{aligned} \tag{4}$$

where Γ is the boundary of the domain Ω and n_i is the i -th component of the outward normal vector \mathbf{n} to the boundary Γ . The function $G = G(\mathbf{x}, \mathbf{y})$ is the fundamental solution of potential problem and can be expressed as

$$G = \frac{1}{2\pi} \ln \frac{1}{r}, \tag{5}$$

$$\frac{\partial G}{\partial x_i} = -\frac{r_i}{2\pi r}, \tag{6}$$

where r is the distance between the source point \mathbf{y} and the field point \mathbf{x} . $r_i = \partial r / \partial x_i = (x_i - y_i) / r$.

Using the property of Dirac delta function, the last domain integral of Eq. (4) can be written as

$$\int_{\Omega} \lambda T \frac{\partial}{\partial x_i} \left(\frac{\partial G}{\partial x_i} \right) d\Omega = -\lambda(\mathbf{y})T(\mathbf{y}, t). \quad (7)$$

Substitute Eq. (7) into Eq. (4) and the result into Eq. (3)

$$\begin{aligned} c_i \tilde{T}(\mathbf{y}, t) = & - \int_{\Gamma} G q(\mathbf{x}, t) d\Gamma(\mathbf{x}) - \int_{\Gamma} \tilde{T}(\mathbf{x}, t) \frac{\partial G}{\partial n} d\Gamma(\mathbf{x}) \\ & + \int_{\Omega} V(\mathbf{x}, \mathbf{y}) \tilde{T}(\mathbf{x}, t) d\Omega(\mathbf{x}) - \int_{\Omega} G \tilde{\rho} \frac{\partial \tilde{T}(\mathbf{x}, t)}{\partial t} d\Omega(\mathbf{x}), \end{aligned} \quad (8)$$

where $q(\mathbf{x}, t)$ is the heat flux, c_i is the singularity coefficient. $\tilde{T}(\mathbf{x}, t)$ and $\tilde{\lambda}(\mathbf{x})$ are the normalized temperature and thermal conductivity, which can be expressed as

$$q(\mathbf{x}, t) = -\lambda(\mathbf{x}) \frac{\partial T(\mathbf{x}, t)}{\partial x_i} n_i = -\lambda(\mathbf{x}) \frac{\partial T(\mathbf{x}, t)}{\partial \mathbf{n}}, \quad (9)$$

$$V(\mathbf{x}, \mathbf{y}) = \frac{\partial G}{\partial x_i} \frac{\partial \tilde{\lambda}(\mathbf{x})}{\partial x_i}, \quad (10)$$

$$\tilde{T}(\mathbf{x}, t) = \lambda(\mathbf{x})T(\mathbf{x}, t), \quad (11)$$

$$\tilde{\lambda}(\mathbf{x}) = \ln \lambda(\mathbf{x}), \quad (12)$$

$$\tilde{\rho} = \frac{\rho c}{\lambda(\mathbf{x})}. \quad (13)$$

There are two domain integrals involved in Eq. (8). The domain integrals can be transformed into boundary integrals by using the RIM. Using a collocation technique, a system equation can be obtained

$$\mathbf{H}\tilde{\mathbf{T}} - \mathbf{G}\mathbf{q} = \mathbf{V}\tilde{\mathbf{T}} - \mathbf{C}\dot{\tilde{\mathbf{T}}}, \quad (14)$$

where $\mathbf{H}, \mathbf{G}, \mathbf{V}$ and \mathbf{C} are coefficient matrices of the BEM. $\tilde{\mathbf{T}}$ and $\dot{\tilde{\mathbf{T}}}$ are the normalized temperature vector and its time derivative vector, respectively. It should be noted that the domain integrals in Eq. (8) have been put into the right terms in Eq. (14). To solve the problem with respect to time, a linear approximation can be proposed for the variation of $\tilde{\mathbf{T}}$ and q . Eq. (14) can be expressed as

$$\mathbf{M}\tilde{\mathbf{T}}^{n+1} - \theta_u \mathbf{G}\mathbf{q}^{n+1} = -\mathbf{N}\tilde{\mathbf{T}}^n + (1 - \theta_u)\mathbf{G}\mathbf{q}^n, \quad (15)$$

where

$$\begin{cases} \mathbf{M} = \theta_u \mathbf{H} - \theta_u \mathbf{V} + \mathbf{C} / \Delta t, \\ \mathbf{N} = (1 - \theta_u)\mathbf{H} - (1 - \theta_u)\mathbf{V} - \mathbf{C} / \Delta t. \end{cases} \quad (16)$$

$\tilde{\mathbf{T}}^n$ and \mathbf{q}^n represent the normalized temperature vector and heat flux vector at the n -th time step. θ_u is the Euler parameter usually taken a value between 0.5 and 1.0.

It should be noted that the normalized temperature vector and heat flux vector at n -th time step are known. The problem can be solved by Eq. (15) in the time marching computation. When all the time steps are fulfilled, the unknown boundary condition and

the normalized internal temperature can be obtained. Then the temperature can be computed by Eq. (11).

3 Inverse problem

As shown in Figure 1, all boundary conditions are known except the shape of inner boundary. The purpose is to identify the boundary shape based on the measured temperature T_{ij} and the computed temperature \hat{T}_{ij} . It should be noted that the measured temperature T_{ij} contains measurement noises.

The solution of the present problem is transformed to find a boundary shape $\mathbf{p}(\theta)$ by minimizing the objective function

$$J(\mathbf{p}(\theta)) = \sum_{i=1}^w \sum_{j=1}^m (T_{ij} - \hat{T}_{ij})^2, \quad (17)$$

where w is the number of measurement timepoints (the important moments among the whole computation time) and m is the number of measurement points. The basic principle of selecting the timepoints is that if the temperature of measurement points changes obviously during a time interval $[t_i, t_{i+1}]$, the time point t_{i+1} is selected. The values of \hat{T}_{ij} can be obtained by solving the direct problem with the estimated boundary shape $\mathbf{p}(\theta)$.

As the unavoidable measurement noises or the numerical computing errors, the first order regularization can be used to avoid instabilities in the estimated values. The objective function is defined as

$$J(\mathbf{p}(\theta)) = \sum_{i=1}^w \sum_{j=1}^m (T_{ij} - \hat{T}_{ij})^2 + \gamma \sum_{k=1}^n (p'_k(\theta))^2, \quad (18)$$

where n is the number of observation points. γ is the regularization parameter, which can minimize the instabilities and effect of noisy data. Selection of an appropriate value of γ is crucial for the shape identification problems. L-shape curve method is suitable for obtaining the regularization parameter [Udayraj, Mulani and Talukdar et al. (2015)].

4 CS-CGM method

4.1 CS algorithm

The CS is a metaheuristic algorithm by mimicking cuckoos. The aggressive behavior of cuckoos is that they lay eggs in the nests of other species [Payne and Sorensen (2005)]. Therefore, it has a chance that the host of the nest will discover the cuckoo's eggs and abandon the eggs or nest. So, some cuckoo species simulate the eggs of the host nest in color or in pattern. This reduces the possibility of the dropped eggs and increases their reproductively.

Usually, there are three idealized rules in the CS:

- (1) A laid egg by each cuckoo puts in an arbitrarily selected nest at a time;

- (2) The next generations go on with the best nests (good quality eggs);
- (3) The egg laid by cuckoo is searched by the host bird from the fixed number of host nests with a probability $P_a \in [0,1]$. In this way, new random solutions (new nests) can replace the host nests.

The purpose of the CS is to find \mathbf{p} which minimizes the objective function $J(\mathbf{p})$. The new solution $\mathbf{p}^{(k+1)}$ can be obtained by the above equations for the k -th iteration

$$\mathbf{p}_i^{(k+1)} = \mathbf{p}_i^{(k)} + \partial_0 \oplus \text{Lévy}(\varphi), \tag{19}$$

where ∂_0 is a constant which should be related to the scales of the problem of interests (in this paper $\partial_0 = 1$). φ is the Lévy exponent, in this paper $\varphi = 1.5$. The product \oplus means entry-wise multiplications.

Usually, the foraging behavior of animals is random or quasi-random and the behavior has demonstrated the characteristics of Lévy flight. The random walk and step can be generated by the Lévy flight according to the distribution

$$\text{Lévy} \sim u = k^{-\varphi}, \tag{20}$$

where u is the normal stochastic variable, k is the number of iterations.

In order to generate random numbers which, obey Lévy flights, a step size and a random direction must be computed by the given Lévy distribution. The step can be expressed as

$$\mu = \frac{u}{|v|^{\frac{1}{\varphi}}}, \tag{21}$$

v is the normal stochastic variable. u and v obey the normal distribution and can be written as

$$u \sim N(0, \sigma_u^2) \text{ and } v \sim N(0, \sigma_v^2), \tag{22}$$

$$\sigma_u = \left\{ \frac{\Gamma(1 + \varphi) \cdot \sin\left(\frac{\varphi}{2} \pi\right)}{\Gamma\left[\left(\frac{1 + \varphi}{2}\right) \cdot \varphi \cdot 2^{\frac{\varphi-1}{2}}\right]} \right\}^{\frac{1}{\varphi}}, \quad \sigma_v = 1,$$

(22)

where $\Gamma(z)$ is a gamma function given by

$$\Gamma(z) = \int_0^\infty k^{z-1} e^{-k} dk. \tag{23}$$

Obviously, each egg in the host nest has a chance to be found by the host bird and the possibility of finding is P_a . Once found, a new nest will be built near the old one

$$p_i^{(k)} = p_i^{(k)} + \chi(p_i^{(k)} - p_j^{(k)}), \tag{24}$$

where χ is a number following the normal distribution with the range in 0 to 1.

4.2 Conjugate gradient method

The iterative process based on the CGM to solve the IGP can be expressed as follows

$$\mathbf{p}^{(k+1)}(\theta) = \mathbf{p}^{(k)}(\theta) - \psi^{(k)} \mathbf{P}^{(k)}(\theta), \quad (25)$$

where $\psi^{(k)}$ is the search step size in the iterative process from the iteration k to $k+1$. $\mathbf{P}^{(k)}(\theta)$ is the direction of descent and given as

$$\mathbf{P}^{(k)}(\theta) = \nabla J(\mathbf{p}^{(k)}(\theta)) + \tau^{(k)} \mathbf{P}^{(k-1)}(\theta), \quad (26)$$

where $\nabla J(\mathbf{p}^{(k)}(\theta))$ is the conjugation of the gradient direction. The conjugate coefficient $\tau^{(k)}$ at the iteration k is determined from the following relation

$$\tau^{(k)} = \begin{cases} \frac{\nabla J(\mathbf{p}^{(k)}(\theta)) \nabla J^T(\mathbf{p}^{(k)}(\theta))}{\nabla J(\mathbf{p}^{(k-1)}(\theta)) \nabla J^T(\mathbf{p}^{(k-1)}(\theta))}, & k \geq 1 \\ 0, & k = 0 \end{cases} \quad (28)$$

where ∇J is defined as follows

$$\nabla J = \left[\frac{\partial J(\mathbf{p}(\theta))}{\partial p_1}, \frac{\partial J(\mathbf{p}(\theta))}{\partial p_2}, \dots, \frac{\partial J(\mathbf{p}(\theta))}{\partial p_n} \right]. \quad (29)$$

The search step size $\psi^{(k)}$ in Eq. (25) is given as

$$\psi^{(k)} = \frac{\sum_{i=1}^w \sum_{j=1}^m ((T_{ij} - \hat{T}_{ij}) \nabla T_{ij} \cdot \mathbf{P}^{(k)})}{\sum_{i=1}^w \sum_{j=1}^m (\nabla T_{ij} \cdot \mathbf{P}^{(k)})^2}. \quad (30)$$

In this paper, the following stopping criterion is taken for the inverse problem $J(\mathbf{p}(\theta)) < \varepsilon$, (31)

where ε is an arbitrary small positive number.

4.3 CS-CGM method

Although the CS is a novel global optimization method, the convergence speed of the CS is very slow because the search direction and iteration step do not utilize the gradient information. In this paper, the method combining the CS with the CGM is proposed to identify the pipe's inner surface. After implement of Lévy flights and elimination mechanism, the values of objective function are decreased rapidly by using the CGM. As a result, the local search ability of the CS-CGM method is significantly strengthened.

The computation process of the CS-CGM for solving the shape identification problem is summarized and the flowchart is shown in Figure 2.

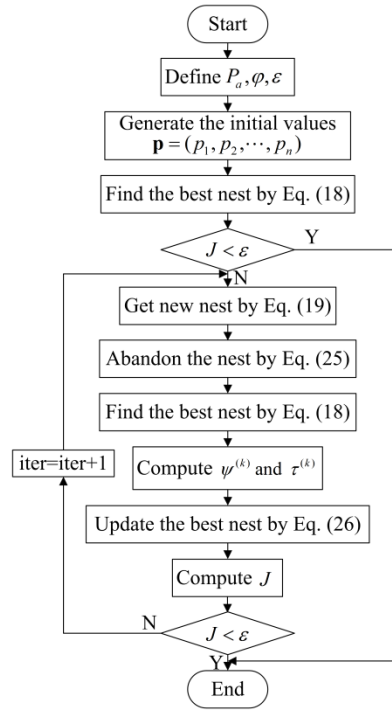


Figure 2: The flowchart of the CS-CGM

5 Numerical example

Four numerical examples are presented to prove the accuracy and effectiveness of the three methods in this section. In order to compare the results with random measurement noises, normally distributed uncorrelated errors with zero and constant standard deviation are assumed. The measurement temperature \mathbf{T} can be expressed as

$$\mathbf{T} = \mathbf{T}^* + \omega\sigma, \tag{32}$$

where \mathbf{T}^* is the solution of the direct problem with the exact boundary shape and σ is the standard deviation. ω is a random variable generated by RAND subroutine of MATLAB. The generated ω belongs to the interval $[-1, 1]$.

In order to check the convergence of the three methods, an average relative error (ARE) is given as follows

$$ARE = \sqrt{\frac{1}{n} \sum_{i=1}^n \frac{(p_{est,i} - p_{exa,i})^2}{p_{exa,i}^2}}, \tag{33}$$

where n denotes the number of observation points. $p_{est,i}$ and $p_{exa,i}$ represent the estimate shape and the exact shape of the i -th node, respectively.

As shown in Figure 3, the outer radius is 2 m. The temperature of the outside

environment and the initial temperature are given as $T_\infty = T_0 = 0^\circ\text{C}$. The heat is transferred from the outer surface to the air by natural convection and the temperature distribution on the inner boundary is $\bar{T} = 100^\circ\text{C}$ at $t=0$. The coefficient of convective heat transfer $h = 20\text{W}/(\text{m}^2 \cdot ^\circ\text{C})$. The specific heat $c = 871\text{J}/(\text{kg} \cdot ^\circ\text{C})$, the density $\rho = 271\text{kg}/\text{m}^3$. The direct problem is solved by the RIBEM. The inner and outer boundaries are divided into 16 linear elements, respectively. The whole computation time is 200 s and the time interval is $\Delta t = 0.01\text{s}$. 16 observation points are chosen coinciding with the corresponding nodes of 16 linear elements on the inner boundary. And the measurement points are uniformly located on the cycle $R=1.8\text{ m}$. The stopping criterion is taken as $\varepsilon = 0.1$.

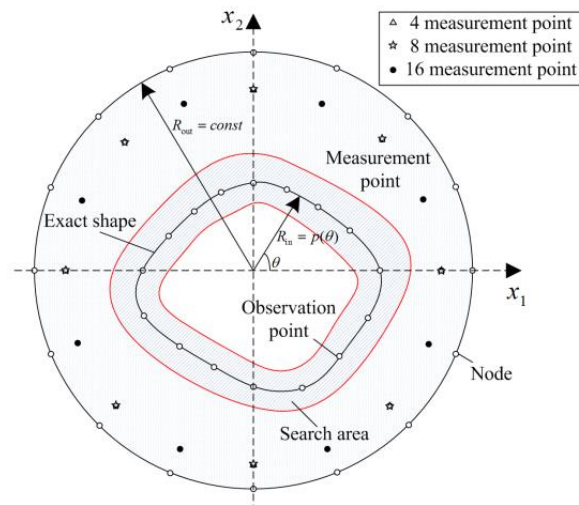


Figure 3: BEM model of the pipe

5.1 Circle inner boundary

The exact shape of the inner wall in this example is a cycle with the radius $R=1\text{ m}$. And the thermal conductivity $\lambda = (200 + 10x_1)\text{W}/(\text{m} \cdot ^\circ\text{C})$.

5.1.1 The effect of initial guess

The problem is solved by the CS, CGM and CS-CGM with different initial values. In this case, the number of measurement timepoints is taken as 2. The inverse results are listed in Table 1. It can be seen that when the initial boundary shape is closer to the exact shape, satisfactory results can be obtained by the CGM. However, the results of the CGM are very sensitive to the initial values and the CGM cannot converge when the initial value is taken as 0.5 or 1.5. In the CS and CS-CGM, the initial values are generated by the random numbers from 0.3 to 1.5. The CS-CGM can obtain satisfactory results by less iteration number. However, the CS needs more iterations and costs more computation time. The results show that the CS-CGM has higher convergence efficiency than the CS and the CGM.

Table 1: Comparison of CS, CGM and CS-CGM.

	Initial guess	Number of iterations	$J(\mathbf{p})$	ARE
CS	[0.3,1.5]	380	9.870e-2	2.882e-2
	0.5	20	3.391e3	-
CGM	0.8	10	9.884e-2	2.507e-2
	1.2	9	1.230e-2	2.279e-2
	1.5	20	1.971e4	-
CS-CGM	[0.3,1.5]	7	7.261e-2	1.041e-2

5.1.2 The effect of the number of measurement timepoints

For comparison, the numbers of measurement timepoints are taken as 1, 2 and 4, respectively. The inverse results of the CS, CGM and CS-CGM are shown in Figure 4 and the AREs are listed in Table 2.

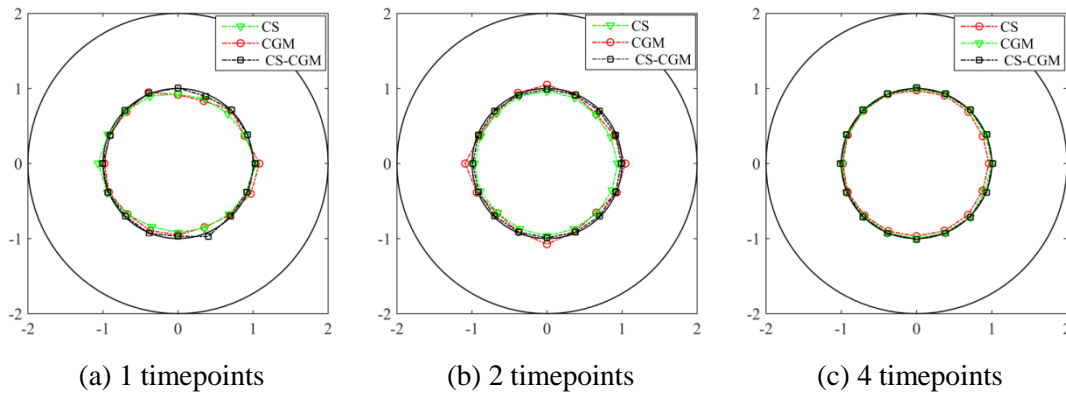


Figure 4: Inverse results with different timepoints

Table 2: AREs for different timepoints

Number of timepoints	CS	CGM	CS-CGM
1	5.429e-2	5.408e-2	2.512e-2
2	5.161e-2	4.762e-2	1.041e-2
4	2.846e-2	7.324e-3	1.097e-2

From Figure 4, it can be seen that the CS, CGM and CS-CGM can identify the pipe's inner surface with different numbers of timepoints. As the number of timepoints increases, the estimated shape is closer to the exact shape. The results of the CGM and CS-CGM are better than the CS. Table 2 shows that with the increase of number of timepoints, the AREs are getting smaller. Next, the number of measurement timepoints is taken as 2.

5.2 Eccentric circle inner boundary

In this example, the inner boundary shape is an eccentric circle with

$$R = 1 + 0.3\sin(\theta + \pi/8). \text{ The thermal conductivity } \lambda = (200 + 10x_1) \text{ W}/(\text{m} \cdot ^\circ \text{C}).$$

5.2.1 The effect of the number of measurement points

As shown in Figure 3, the numbers of measurement points are taken as $m=4, 8$ and 16 . The inverse results obtained by the CS, CGM and CS-CGM are shown in Figure 5 and the AREs are listed in Table 3.

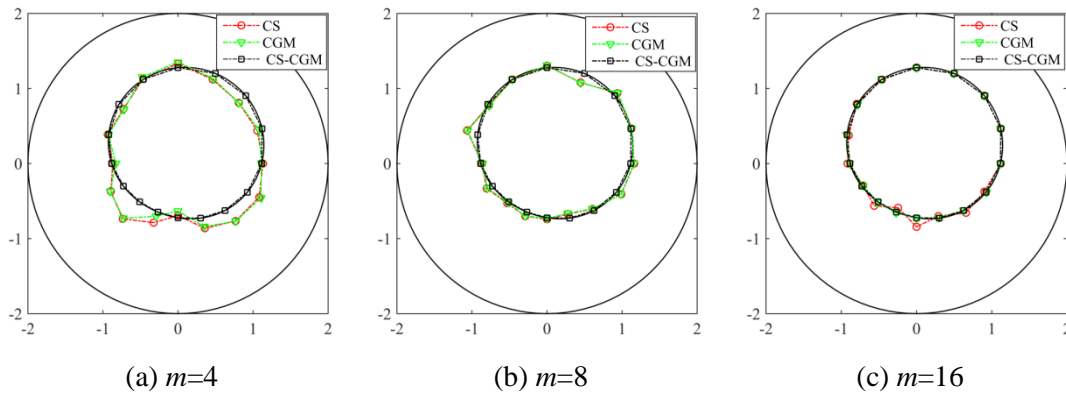


Figure 5: Inverse results with different measurement points

Table 3: AREs for different measurement points

Number of measurement points	CS	CGM	CS-CGM
$m=4$	1.306e-1	1.286e-1	1.225e-1
$m=8$	6.386e-2	6.309e-2	3.229e-2
$m=16$	4.096e-2	6.579e-3	1.013e-2

From Figure 5, it is clear that when the number of measurement points $m=4$, only the CS-CGM can get accurate results. When the number of measurement points is taken as 16, the results obtained by the CGM and CS-CGM are better than the CS. It is clear to see that as the number of measurement points increases, the inverse shape is closer to the exact shape. Table 3 shows that the AREs decrease with the increase of measurement point number.

5.2.2 The effect of random noises

In order to test the stability of the three methods, the measurement noises are taken as 1.0%, 2.0% and 3.0%. For comparison, the number of measurement points is taken as $m=16$. The inverse results with different measurement noises are exhibited in Figure 6. Table 4 provides the AREs corresponding to the measurement noises.

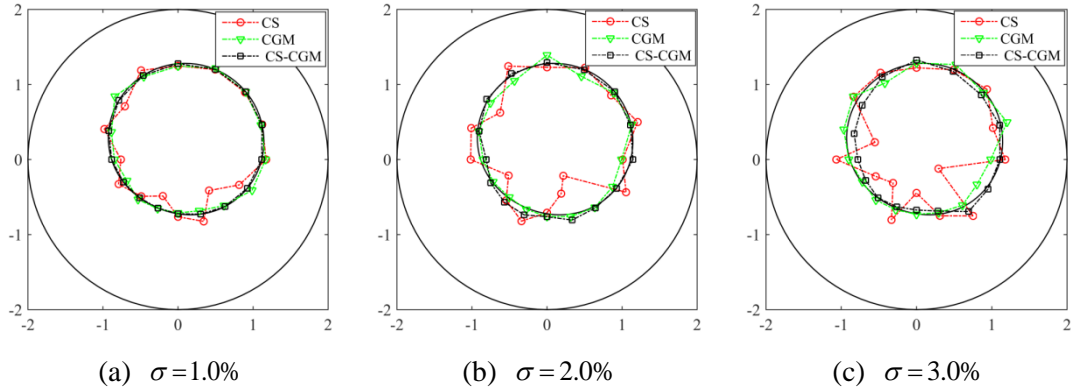


Figure 6: Inverse results with different measurement noises

Table 4: AREs for different measurement noises

Measurement noises	CS	CGM	CS-CGM
$\sigma = 1.0\%$	1.077e-1	4.019e-2	3.564e-2
$\sigma = 2.0\%$	1.988e-1	6.399e-2	6.612e-2
$\sigma = 3.0\%$	2.364e-1	7.144e-2	7.606e-2

From Figure 6, it is found that with the increase of measurement noises, the results are diverging from the exact shape. When the measurement noise is taken as 3.0%, the results of the CS-CGM are better than the CS. As shown in Table 4, with the decrease of measurement noises, the AREs are getting smaller. It is clear to see that the results obtained by the CS algorithm are more sensitive to the measurement noises than the CGM and CS-CGM.

5.3 The nephroid inner boundary

In this example, the inner boundary shape is considered as an irregular geometry with

$$R = \sqrt{(0.8\cos(\theta))^2 + (1.3\sin(\theta))^2} .$$

The thermal conductivity $\lambda = (200 + 10\sqrt{x_1^2 + x_2^2}) \text{W}/(\text{m} \cdot ^\circ \text{C})$.

5.3.1 The effect of the number of measurement points

In this case, the numbers of measurement points are also taken as 4, 8 and 16. The inverse results of the CS, CGM and CS-CGM are shown in Figure 7. It is clear that the CS, CGM and CS-CGM can identify the inner shape. The results get more accurate as the measurement points increase. When sufficient measurement information is used, satisfactory results can be obtained.

The AREs with different number of measurement points are also computed and listed in Table 5. With the increase of number of measurement points, the inverse results are

closer to the exact ones and the AREs get smaller. It shows that the results obtained by the CS-CGM are more accurate than the CS and CGM.

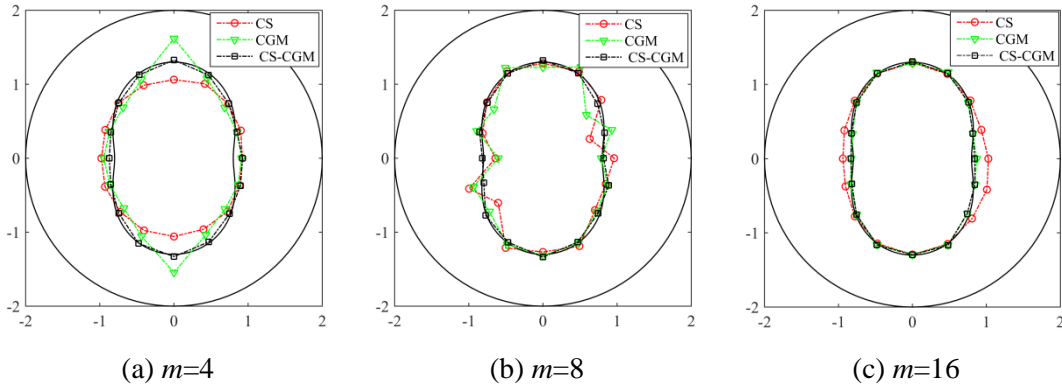


Figure 7: Inverse results with different measurement points

Table 5: AREs for different measurement points

Number of measurement points	CS	CGM	CS-CGM
$m=4$	1.429e-1	1.334e-1	5.496e-2
$m=8$	1.154e-1	1.055e-1	2.707e-2
$m=16$	1.089e-1	2.935e-2	2.112e-2

5.3.2 The effect of random noises

The measurement noises are taken as 1.0%, 2.0% and 3.0%. In this case, 16 measurement points are considered. The inverse results with different measurement noises are displayed in Figure 8. Table 6 provides the AREs corresponding to the measurement noises.

From Figure 8, it is found that with the increase of measurement noises, the results are diverging from the exact shape. When the measurement noise is taken as 3.0%, the results obtained by the CS-CGM are better than the CS and CGM. As shown in Table 6, with the decrease of measurement noises, the AREs are smaller and the estimated shape is closer to the exact one. The results show that the measurement noise has less effect on the results of the CGM and CS-CGM.

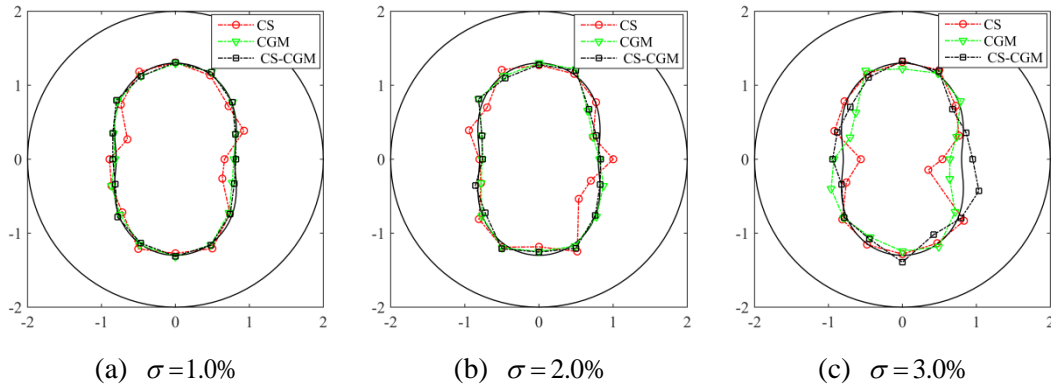


Figure 8: Inverse results with different measurement noises

Table 6: AREs for different measurement noises

Measurement noises	CS	CGM	CS-CGM
$\sigma = 1.0\%$	9.755e-2	2.812e-2	2.575e-2
$\sigma = 2.0\%$	1.280e-1	6.086e-2	5.597e-2
$\sigma = 3.0\%$	1.709e-1	1.143e-1	1.048e-1

5.4 The square inner boundary

In this example, a square inner shape is considered. The length of the side is 2 m. The thermal conductivity $\lambda = (200 + 10\sqrt{x_1^2 + x_2^2}) \text{W}/(\text{m} \cdot ^\circ \text{C})$.

5.4.1 The effect of the number of measurement points

In this case, three different kinds of measurement points are also considered. The inverse results of the CS, CGM and CS-CGM are shown in Figure 9. The AREs with different measurement points are given in Table 7.

From Figure 9, it is clear that the CS, CGM and CS-CGM can identify the inner shape with 16 measurement points. As listed in Table 7, with the increase of number of measurement points, the inverse results are closer to the exact ones and the AREs get smaller. It shows that the results obtained by the CS-CGM are more accurate than the CS and CGM.

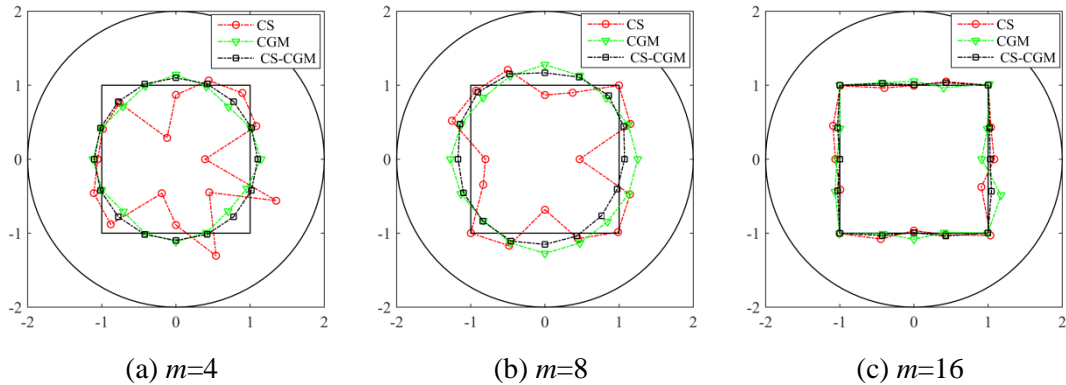


Figure 9: Inverse results with different measurement points

Table 7: AREs for different measurement points

Number of measurement points	CS	CGM	CS-CGM
$m=4$	4.053e-1	2.152e-1	1.973e-1
$m=8$	2.369e-1	1.973e-1	1.474e-1
$m=16$	5.557e-2	6.101e-2	1.140e-2

5.4.2 The effect of random noises

The measurement noises are also taken as 1.0%, 2.0% and 3.0%. 16 measurement points are used. The inverse results are displayed in Figure 10. Table 8 provides the AREs.

From Figure 10, it is found that with the increase of measurement noises, the results are diverging from the exact shape. When the measurement noise is taken as 3.0%, the results obtained by the CS-CGM are better than the CS and CGM. As shown in Table 8, with the decrease of measurement noises, the AREs are smaller and the estimated shape is closer to the exact one.

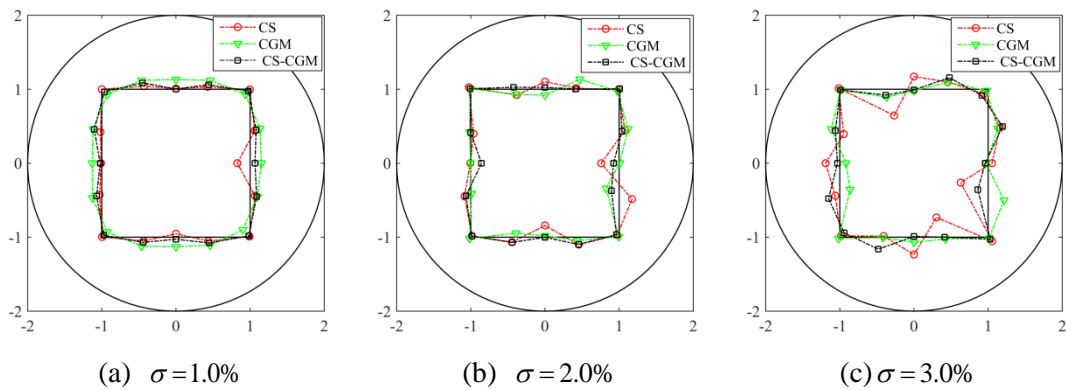


Figure 10: Inverse results with different measurement noises

Table 8: AREs for different measurement noises

Measurement noises	CS	CGM	CS-CGM
$\sigma = 1.0\%$	6.229e-2	1.124e-1	4.695e-2
$\sigma = 2.0\%$	1.119e-1	7.775e-1	6.299e-2
$\sigma = 3.0\%$	1.954e-1	8.903e-1	9.794e-2

6 Conclusion

In this paper, the CS is improved by the CGM, and the CS-CGM is proposed. The CS, CGM and CS-CGM are used to predict a pipe's inner-surface in FGMs. The unknown boundary shapes are generated randomly and evolved by Lévy flights and elimination mechanism for the CS and CS-CGM. Then the CGM is adopted to minimize the objective function. The influences of the number of measurement timepoints, measurement points and the random measurement noises on the inverse results are also discussed. It is observed that all the three algorithms are able to estimate the unknown inner boundary shape of the pipe. The computational efficiency of the CS, CGM and CS-CGM is also compared. The followings are the major conclusions:

- (1) The three methods can perform in the case of noiseless measurements for prediction of a pipe's inner surface.
- (2) The results obtained by the CS are more sensitive to the measurement noises compared with the CGM and CS-CGM. To get accurate results, the CS needs more iteration numbers.
- (3) The CGM has good performance in the identification of the pipe's inner surface. But the CGM is very sensitive to initial values.
- (4) The CS-CGM has the best efficiency and the fastest convergence speed among the three methods.
- (5) With the increase of timepoints and measurement points, and with the decrease of measurement noise, the inverse results are more accurate.

It can be concluded that the CS-CGM is better than the CS and CGM. Therefore, the CS-CGM can be used to satisfactorily identify the inner shape of a pipe in engineering.

Acknowledgements: The research is supported by the National Natural Science Foundation of China (Nos. 11672098, 11502063) and the Natural Science Foundation of Anhui Province (No. 1608085QA07).

References

- Alifanov, O. M.** (1994): *Inverse heat transfer problems*, Springer-Verlag, Berlin Heidelberg.
- Abreu, A. I.; Canelas, A.; Mansur, W. J.** (2013): A CQM-based BEM for transient heat conduction problems in homogeneous materials and FGMs. *Applied Mathematical Modelling*, vol. 37, pp. 776-792.

AL-Jawary, M. A.; Wrobel, L. C. (2012): Radial integration boundary integral and integro-differential equation methods for two-dimensional heat conduction problems with variable coefficients. *Engineering Analysis with Boundary Elements*, vol. 36, pp. 685-695.

Cheng, C. H.; Chang, M. H. (2003): Shape identification by inverse heat transfer method. *Transactions-American Society of Mechanical Engineers Journal of Heat Transfer*, vol. 125, pp. 224-231.

Chen, B.; Chen, W.; Wei, X. (2015): Characterization of space-dependent thermal conductivity for nonlinear functionally graded materials. *International Journal of Heat and Mass Transfer*, vol. 84, pp. 691-699.

Chen, H.; Cao, D. M.; Wang, G. J.; Wan, S. B.; Li, Y. H. (2016): Fuzzy estimation for unknown boundary shape of fluid-solid conjugate heat transfer problem. *International Journal of Thermal Sciences*, vol. 106, pp. 112-121.

Fu, Z. J.; Chen, W.; Yang, H. T. (2013): Boundary particle method for Laplace transformed time fractional diffusion equations. *Journal of Computational Physics*, vol. 235, pp. 52-66.

Fu, Z. J.; Chen, W.; Zhang, C. Z. (2012): Boundary particle method for Cauchy inhomogeneous potential problems. *Inverse problems in Science and Engineering*, vol. 20, pp. 189-207.

Fan, C. L.; Sun, F. R.; Yang, L. (2007): An algorithm study on the identification of a pipeline's irregular inner boundary based on thermographic temperature measurement. *Measurement Science and Technology*, vol. 18, pp. 2170-2177.

Gao, X. W. (2002): The radial integration method for evaluation of domain integrals with boundary-only discretization. *Engineering Analysis with Boundary Elements*, vol. 26, pp. 905-916.

Gao, X. W. (2005): Evaluation of regular and singular domain integrals with boundary-only discretization-theory and Fortran code. *Journal of Applied Mathematics and Computing*, vol. 175, pp. 265-290.

Girish, K.; Hema, S. (2016): Analytical estimation of radar cross section of infinitely long conducting cylinder coated with metamaterial. *Computers, Materials & Continua*, vol. 52, pp. 193-211.

Gao, X. W.; Zhang, C.; Guo, L. (2007): Boundary-only element solutions of 2D and 3D nonlinear and nonhomogeneous elastic problems. *Engineering Analysis with Boundary Elements*, vol. 31, pp. 974-982.

Gao, X. W.; Zheng, B. J.; Yang, K.; Zhang, C. (2015): Radial integration BEM for dynamic coupled thermoelastic analysis under thermal shock loading. *Computers & Structures*, vol. 158, pp. 140-147.

Huang, C. H.; Liu, C. Y. (2010): A three-dimensional inverse geometry problem in estimating simultaneously two interfacial configurations in a composite domain. *International Journal of Heat and Mass Transfer*, vol. 53, pp. 48-57.

Hafid, M.; Lacroix, M. (2017): Inverse heat transfer prediction of the state of the brick wall of a melting furnace. *Applied Thermal Engineering*, vol. 110, pp. 265-274.

Kazemzadeh-Parsi, M. J.; Daneshmand, F. (2013): Inverse geometry heat conduction

analysis of functionally graded materials using smoothed fixed grid finite elements. *Inverse Problems in Science and Engineering*, vol. 21, pp. 235-250.

Karageorghis, A.; Lesnic, D.; Marin, L. (2015): The method of fundamental solutions for solving direct and inverse Signorini problems. *Computers & Structures*, vol. 151, pp. 11-19.

Li, G. Y.; Guo, S. P.; Zhang, J. M.; Li, Y.; Han, L. (2015): Transient heat conduction analysis of functionally graded materials by a multiple reciprocity boundary face method. *Engineering Analysis with Boundary Elements*, vol. 60, pp. 81-88.

Lee, H. L.; Lai, T. H.; Chen, W. L.; Yang, Y. C. (2013): An inverse hyperbolic heat conduction problem in estimating surface heat flux of a living skin tissue. *Applied Mathematical Modelling*, vol. 37, pp. 2630-2643.

Li, Y. H.; Wang, G. J.; Chen, H.; Zhu, Z. Y.; Zhang, D. Q. (2016): A decentralized fuzzy inference method for the inverse geometry heat conduction problem. *Applied Thermal Engineering*, vol. 106, pp. 109-116.

Naumann, D. S.; Evans, B.; Walton, S.; Hassan, O. (2015): A novel implementation of computational aerodynamic shape optimisation using modified cuckoo search. *Applied Mathematical Modelling*, vol. 40, pp. 4543-4559.

Naumann, D. S.; Evans, B.; Walton, S.; Hassan, O. (2016): A novel implementation of computational aerodynamic shape optimisation using modified cuckoo search. *Applied Mathematical Modelling*, vol. 40, pp. 4543-4559.

Nguyen, T. T.; Vo, D. N.; Truong, A. V. (2014): Cuckoo search algorithm for short-term hydrothermal scheduling. *Applied Energy*, vol. 132, pp. 276-287.

Partridge, P. W.; Brebbia, C. A.; Wrobel, L. C. (1992): The dual reciprocity boundary element method, Computational Mechanics Publication, Southampton.

Payne, R. B.; Sorensen, M. D. (2005): *The cuckoos*, Oxford University Press, Oxford.

Partridge, P. W.; Wrobel, L. C. (2007): An inverse geometry problem for the localisation of skin tumours by thermal analysis. *Engineering Analysis with Boundary Elements*, vol. 31, pp. 803-811.

Rus, G.; Gallego, R. (2002): Optimization algorithms for identification inverse problems with the boundary element method. *Engineering Analysis with Boundary Elements*, vol. 26, pp. 315-327.

Sun, X. S.; Huang, L. X.; Liu, Y. H.; Cen, Z. Z. (2004): Elasto-plastic analysis of two-dimensional orthotropic bodies with the boundary element method. *Computers, Materials & Continua*, vol. 1, pp. 91-105.

Sladek, J.; Sladek, V.; Zhang, C. (2004): A local BIEM for analysis of transient heat conduction with nonlinear source terms in FGMs. *Engineering Analysis with Boundary Elements*, vol. 28, pp. 1-11.

Sun, S. C.; Hong, Q.; Zhao, F. Z.; Ruan, L. M.; Li, B. X. (2016): Inverse geometry design of two-dimensional complex radiative enclosures using Krill Herd optimization algorithm. *Applied Thermal Engineering*, vol. 98, pp. 1104-1115.

Taler, J.; Duda, P. (2006): *Solving direct and inverse heat conduction problems*, Springer-Verlag, Berlin Heidelberg.

Tadeu, A.; Prata, J.; Simões, N. (2015): Dynamic simulation of three-dimensional heat conduction through cylindrical inclusions using a BEM model formulated in the frequency domain. *Applied Mathematics and Computation*, vol. 261, pp. 397-407.

Udayraj; Mulani, K.; Talukdar, P.; Das, A.; Alagirusamy, R. (2015): Performance analysis and feasibility study of ant colony optimization, particle swarm optimization and cuckoo search algorithms for inverse heat transfer problems. *International Journal of Heat and Mass Transfer*, vol. 89, pp. 359-378.

Valian, E.; Tavakoli, S.; Mohanna, S.; Haghi, A. (2013): Improved cuckoo search for reliability optimization problems. *Computers & Industrial Engineering*, vol. 64, pp. 459-468.

Wu, C. H.; Jiang, R. Y. (2015): Three-dimensional free vibration analysis of sandwich FGM cylinders with combinations of simply-supported and clamped edges and using the multiple time scale and meshless methods. *Computers, Materials & Continua*, vol. 46, pp. 17-56.

Wang, S. H.; Lin, S. C.; Yang, Y. C. (2015): Geometry estimation for the inner surface in a furnace wall made of functionally graded materials. *International Communications in Heat and Mass Transfer*, vol. 67, pp. 1-7.

Yang, X. S.; Deb, S. (2009): Cuckoo search via Lévy flights. *NaBIC 2009*, World Congress on IEEE, Coimbatore, December 9-11, pp. 210-214.

Yang, X. S.; Deb, S. (2010): Engineering optimisation by cuckoo search. *International Journal of Mathematical Modelling and Numerical Optimisation*, vol. 1, pp. 330-343.

Yu, B.; Zhou, H.L.; Chen, H. L.; Tong, Y. (2015): Precise time-domain expanding dual reciprocity boundary element method for solving transient heat conduction problems. *International Journal of Heat and Mass Transfer*, vol. 91, pp. 110-118.

Zhang, X. M.; Yu, J. G.; Zhang, M.; Zhang, D. P. (2015): Guided waves in functionally graded rods with rectangular cross-section under initial stress. *Computers, Materials & Continua*, vol. 48, pp. 163-179.